

Real-Time Structural and Optical Study of Growth and Packing Behavior of Perylene Diimide Derivative Thin Films: Influence of Side-Chain Modification

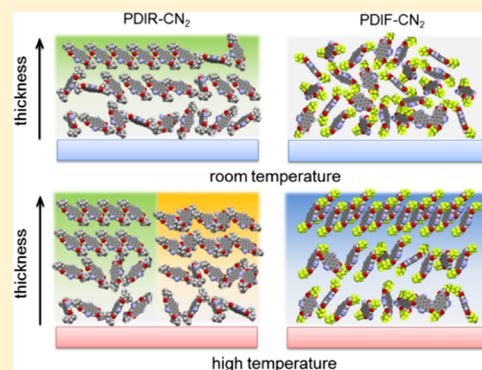
Valentina Belova,^{*,†,‡} Benjamin Wagner,[†] Berthold Reisz,[†] Clemens Zeiser,[†] Giuliano Duva,[†] Jakub Rozbořil,[‡] Jiří Novák,[‡] Alexander Gerlach,[†] Alexander Hinderhofer,^{*,†,‡} and Frank Schreiber[†]

[†]Institut für Angewandte Physik, Universität Tübingen, Auf der Morgenstelle 10, 72076 Tübingen, Germany

[‡]CEITEC, Masaryk University and Department of Condensed Matter Physics, Faculty of Science, Masaryk University, Kotlářská 2, CZ-611 37 Brno, Czech Republic

Supporting Information

ABSTRACT: We study the growth of two n-type small-molecule organic semiconductors from the perylene diimide family: *N,N'*-bis-(2-ethylhexyl)-dicyanoperylene-3,4:9,10-bis(dicarboximide) (PDIR-CN₂) and *N,N'*-1*H*,1*H*-perfluorobutyl-dicyanoperylene-3,4:9,10-bis(dicarboximide) (PDIF-CN₂) whose chemical structures differ only in the imide substituents, branched alkyl chains –C₈H₁₆ and linear fluoroalkyl chains –C₄F₇H₂, respectively. Both types of substituents introduce some degree of steric hindrance for intermolecular interactions, affecting solid-state packing during thin film formation, and thus induce specific structure-dependent optoelectronic properties in thin films. The transition from an amorphous structure to crystalline domains with strong intermolecular coupling was followed in situ and in real time during growth. We investigated the structural and morphological properties by X-ray diffraction and atomic force microscopy as a function of the substrate temperature and chemical structure. We examined the relationship between the structural properties and thin film optical signatures probed via differential reflectance spectroscopy, ellipsometry, and temperature-dependent photoluminescence. A new crystalline PDIR-CN₂ polymorph at high temperatures emerges. In addition, we observed in PDIF-CN₂ that the fluorinated chains contribute to crystallization inhibition because of the higher overall steric hindrance compared to the alkyl chains.



INTRODUCTION

Organic semiconductors (OSCs) as active layers in organic field-effect transistors (OFETs),^{1–3} organic photovoltaic (OPV) devices,^{4–6} and light-emitting diodes^{7,8} provide not only benefits such as high efficiency, low costs, processability, and device flexibility but also uncountable possibilities for tuning their optoelectronic properties in a controlled way. The most obvious and the most frequently explored approach for this is the modification of their chemical structure. We can distinguish roughly two strategies of molecular modification: (a) a direct change of the electronic properties of the compound, for instance, by fluorination and (b) a change of the geometry of the compound to modify the crystal packing, which has an indirect impact on the film properties.

Fluorination is commonly applied to shift both ionization energy (IE) and electron affinity (EA) to lower energies to create efficient n-type semiconductors with low electron injection barriers and high electron mobilities.^{8–13} Partial fluorination generally improves thermal, air, and photostabilities^{14–16} and can induce noncovalent bonding between fluorinated and nonfluorinated parts and thus favor the crystallization process.^{17–20} Furthermore, the molecular pack-

ing in the solid state is governed by a balance of interactions, including a combination of quadrupolar stabilization, van der Waals forces, and steric requirements.^{21,22} Chemical modification by highly polar substituents or by spacer groups (e.g., side chains) often leads to a change in the intermolecular coupling in solids^{23–28} and in the adsorption behavior on substrates,^{29,30} which in turn determines the device performance.^{31–33} Also, for thin film growth by organic molecular beam deposition (OMBD), the preparation conditions such as the deposition rate, substrate temperature, and base pressure are crucial^{34–36} and have a strong impact on the growth.

In this paper, we present a combined structural and optical study of growth and phase behavior of thin films of perylene diimide (PDI) derivatives representing a well-known family of electron-accepting small molecule OSCs applied as active layers in OFETs^{2,3,37,38} and OPVs.^{39–42} PDIs have demonstrated outstanding chemical and thermal stabilities,⁴³ processability, electron-transport properties, high light absorption capability,

Received: January 23, 2018

Revised: March 20, 2018

Published: March 22, 2018



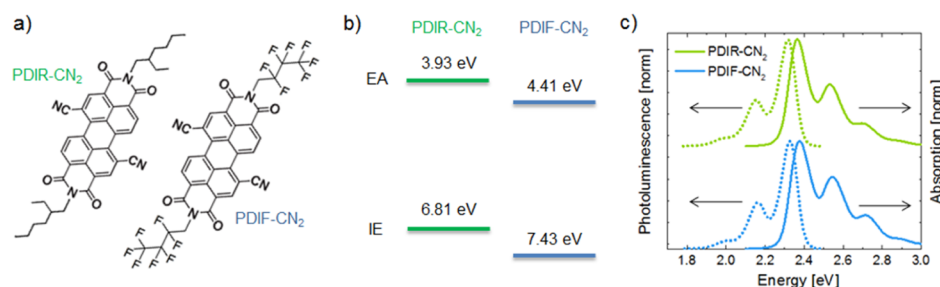


Figure 1. a) Chemical structure of PDIR-CN₂ (C₄₂N₄O₄H₄₀, left) and PDIF-CN₂ (C₃₄N₄O₄F₁₄H₁₀, right); molecule length is 21.2 Å for PDIR-CN₂ and 22.8 Å for PDIF-CN₂; (b) the corresponding IE and EA in thin film; (c) normalized absorption (solid) and photoluminescence (PL) (dotted) spectra in CHCl₃ solution.

and high fluorescence quantum yields,^{26,41} and they hold the promise to surpass fullerenes once a proper functionality control is achieved.^{4,39,44} PDIs consist of a PDI core, responsible for a strong intermolecular π - π interaction driving a cofacial stacking and thus a high tendency to self-assembly, and side substitutions in an imide or bay position, easily changeable by synthesis, which result in a variety of structures and morphologies and consequently physical properties of thin films and devices.⁴⁰ The properties of PDIs containing linear alkyl chain substituents in the imide position [such as *N,N'*-bis(*n*-octyl)-dicyanoperylene-3,4:9,10-bis(dicarboximide), PDI8-CN₂] have already been widely studied in the literature.^{45–47} The linearly configured alkyl chains were found to reveal a minimized steric hindrance and therefore have no distorting impact on molecular packing.²⁸

In the present work, we focus on two variations of PDI compounds: *N,N'*-bis(2-ethylhexyl)-dicyanoperylene-3,4:9,10-bis(dicarboximide) (PDIR-CN₂) with branched alkyl side chains and *N,N'*-1*H*,1*H*-perfluorobutyl-dicyanoperylene-3,4:9,10-bis(dicarboximide) (PDIF-CN₂) with linear fluorinated chains (Figure 1a). These compounds are among the most interesting n-type small-molecule OSCs because of their air stability and high field-effect electron mobilities with reported values in thin films of 0.22 and 0.53 cm²/V·s, respectively, exceeding 0.12 cm²/V·s measured for PDI8-CN₂.^{38,48,49} As one can expect from the high electronegativity of fluorine, the main difference between the two compounds is the energy level shift of PDIF-CN₂ compared with that of PDIR-CN₂. The IE of PDIR-CN₂ in thin films is 6.81 eV and the EA is 3.93 eV. PDIF-CN₂ in thin films has an increased IE of 7.43 eV and an EA of 4.41 eV (Figure 1b). The transport gap in thin films remains nearly identical (2.88 and 3.02 eV, respectively) as well as the monomer optical gap (2.37 and 2.39 eV taken as the lowest peak of a vibronic progression of absorption spectra measured in solution, see Figure 1c), which contrasts with the case of full fluorination.^{50–52} According to density functional theory (DFT) results obtained in several independent studies for this class of OSCs, the highest occupied and lowest unoccupied molecular orbitals of the compounds are concentrated on the PDI core, and therefore, substituents in the imide positions are expected to have only a weak impact on their distribution.^{33,41,44} Hence, the strong change of electronic properties is supposed to stem from the environment in the solid state, that is, the collective anisotropy of the quadrupole moment, while isolated molecules are less affected.⁵³

In contrast to sterically flat and small molecules [e.g., pentacene (PEN),⁵⁴ diindenoperylene (DIP),⁵⁵ sexithiophene (6T),⁵⁶ etc.], the bulky side chains of the studied compounds

hinder intermolecular packing. A real-time growth observation by X-ray diffraction methods allows to follow a transition from nearly uncoupled monomers to highly ordered bulk materials. The thickness-dependent crystallization processes are compared with real-time optical changes recorded by differential reflectance spectroscopy (DRS).⁵⁷ We explore the kinetic growth factors by increasing the substrate temperature and the role of different substituents by comparing growth and packing-dependent coupling behavior of the compounds.

EXPERIMENTAL METHODS

Thin films of PDIR-CN₂ and PDIF-CN₂ (known as ActivInk N1400 and N1100 purchased from Polyera, U.S.A.) were grown by OMBD⁵⁸ with a deposition rate of 0.2 nm/min and a base pressure of 1×10^{-8} mbar (in a portable chamber for real-time experiments)⁵⁹ and 5×10^{-10} mbar (in a stationary chamber for DRS and postgrowth measurements) on top of native silicon oxide (for all experimental techniques), thermally oxidized silicon (for ellipsometry), and backside-roughened quartz glass (for DRS) kept at room temperature (RT) or heated up to 110–160 °C during growth. The film thickness varies from 20 to 30 nm.

X-ray reflectivity (XRR) profiles, grazing incidence X-ray diffraction (GIXD) scans, and reciprocal space maps were measured in situ as well as ex situ after the growth; GIXD was also performed in real time during the growth. Measurements were carried out partly at the European Synchrotron Radiation Facility (ESRF, France) beamline ID10B and partly at the Swiss Light Source (SLS, Switzerland) beamline X04SA.

The film morphology after growth was studied by atomic force microscopy (AFM) using a JPK NanoWizard II setup (JPK Instruments AG, Germany) in the tapping mode.

Optical properties were examined by DRS during growth for real-time investigations and postgrowth by ellipsometry to probe optical anisotropy^{60,61} and by temperature-dependent PL. The DRS setup consists of a fiber-coupled USB2000+ spectrometer and a DH-2000 lamp (Ocean Optics, U.S.A.). Variable angle spectroscopic ellipsometry was performed with a Woollam M2000 ellipsometer (LOT-QuantumDesign GmbH, Germany). PL spectra were measured with a LabRam HR 800 spectrometer (HORIBA Jobin Yvon, France) with a CCD-1024 \times 256-OPEN-3S9 detector and a frequency-doubled Nd:YAG laser (532 nm wavelength). Absorption and fluorescence spectra in ClCH₃ solution were recorded with a Varian Cary UV/vis spectrophotometer (Varian, The Netherlands).

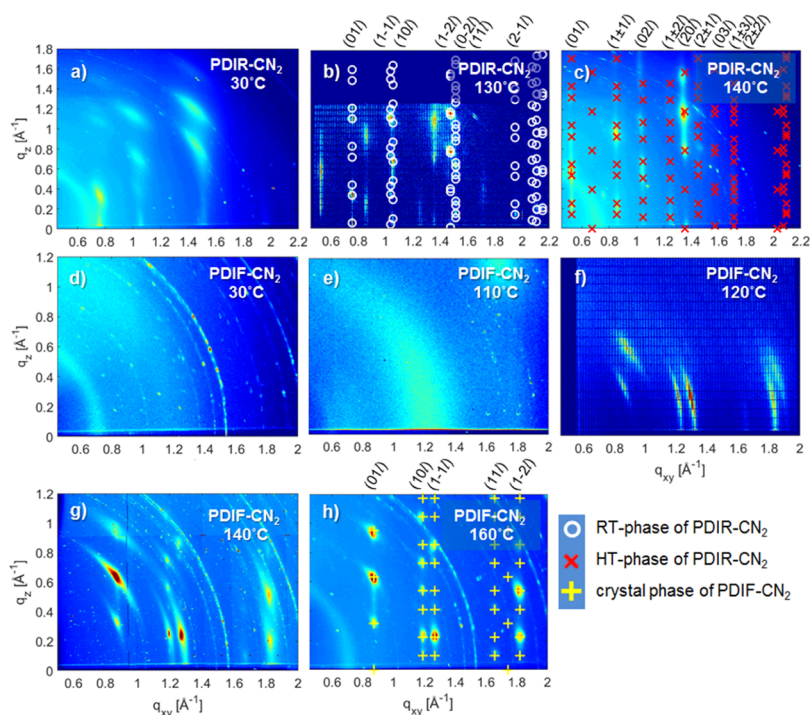


Figure 2. Reciprocal space maps measured postgrowth: (a–c) PDIR-CN₂ and (d–h) PDIF-CN₂ grown at different T_{sub} . Calculated Bragg peak positions (white circles, red crosses, and yellow stars—see legend) are provided without the structure factor and taking the refractive index into account.⁶⁶ For figures (b,c,h), we provide the calculated Miller indices of the corresponding truncation rods on top. The diffraction rings at $q = 0.7 \text{ \AA}^{-1}$ present in (a,c,d,h) and $q = 1.52 \text{ \AA}^{-1}$ present in (d,g,h) are attributed to a Kapton window and a Be window, respectively, and the feature in the upper right corner of (e) is assigned to Si(111).

Table 1. Unit Cell Parameters^a

	a , Å	b , Å	c , Å	α , deg	β , deg	γ , deg	V , Å ³
PDIR-CN ₂ spin-coated ⁶⁵	6.30	8.81	16.56	88.32	84.6	110.63	854.55
PDIR-CN ₂ thin film RT phase (measured at 130 °C)	6.44	8.99	16.59	87.52	86.21	112.55	882.66
PDIR-CN ₂ thin film HT phase	9.33	12.07	16.93	105.24	90	90	1839.49
PDIF-CN ₂ single crystal ⁶⁷	5.23	7.64	18.8	92.51	95.25	104.73	722.52
PDIF-CN ₂ Langmuir–Blodgett monolayer ⁶⁸	5.61	8.05				104.75	
PDIF-CN ₂ thin film (measured at 160 °C)	5.53	7.52	20.4	87.12	101.45	106.31	797.99

^a a and b are parallel to the substrate surface.

RESULTS AND DISCUSSION

Structural Investigation by X-ray Diffraction. One of the main characteristics of PDIs is a strong noncovalent intermolecular interaction favoring one-dimensional (1D) self-assembly in a face-to-face or slipped π – π stacking manner. Numerous kinds of such aggregation motifs (up to liquid crystals) have been widely studied for solution processes,^{62–64} however, the growth behavior during vacuum deposition still remains to be clarified.

Figure 2 shows the reciprocal space maps (q_{xy} is the momentum transfer parallel to the sample surface, whereas q_z is perpendicular to the sample surface) measured postgrowth on thin films of PDIR-CN₂ (Figure 2a–c) and PDIF-CN₂ (Figure 2d–h) grown by OMBD on silicon substrates at different substrate temperatures during deposition.

PDIR-CN₂ deposited at RT (Figure 2a) exhibits a diffraction pattern similar to a spin-coated, annealed film reported by Ferlauto et al.⁶⁵ corresponding to molecules tilted on the surface with a longitudinal displacement. The corresponding unit cell is triclinic and contains one molecule. The same unit cell is observed for films grown at substrate temperatures up to

120 °C. At this temperature, new weak features emerge in addition to the present peaks (see GIXD in Figure S1, Supporting Information). These weak features, which have not been observed before, become more pronounced at higher temperatures ($T_{\text{sub}} = 130 \text{ °C}$, Figure 2b), and they are presumably associated with the nucleation of a yet unreported polymorph. The improved crystallinity at 130 °C gives the opportunity to fit the unit cell parameters (see the white circles marking simulated positions of Bragg reflections in Figure 2b and the corresponding lattice parameters in Table 1). The improvement of crystallinity with increasing temperature followed by an enhancement of charge-transport characteristics was reported for PDIR-CN₂³⁸ as well as for PD18-CN₂,³ a related compound containing a linear alkyl chain. With further increase of the substrate temperature ($T_{\text{sub}} = 140 \text{ °C}$, Figure 2c), the RT-phase almost vanishes and only the new high-temperature (HT)-phase dominates. Red crosses show the fit (Figure 2c) of the HT-phase crystal structure, which results in a monoclinic unit cell with a doubled volume (Table 1) and therefore two molecules per unit cell. We note that the HT polymorph cannot be induced by annealing the RT film (kept

at 130 °C for 1 h, Figure S1, Supporting Information). This observation suggests that more degrees of freedom for intralayer diffusion are required for enabling the phase transition.

In contrast to PDIR-CN₂, the second compound PDIF-CN₂ exhibits only a very weak crystallinity at RT.⁴⁸ In Figure 2d, we observe a weak scattering with an intensity maximum around 1.2 Å⁻¹ in the out-of-plane direction, giving a hint to a weakly ordered lying down preferred molecule orientation (see Figure S2 for the full range *q*-map). With *T*_{sub} elevated up to 110 °C, the diffraction feature is stronger with a maximum in the in-plane direction (Figure 2e). On the basis of the known crystal structure of PDIF-CN₂ single crystal,⁶⁷ the molecules adopt a more standing-up orientation, that is, the tilt angle between the molecular long axis and the substrate normal is small at higher *T*_{sub}.

The Bragg peaks in the *q*_z range below 0.8 Å⁻¹, characteristic of a uniaxially ordered polycrystalline thin film, occur at *T*_{sub} = 120 °C (Figure 2f). Bragg peaks at a higher *q*_z appear at *T*_{sub} = 140 °C (Figure 2g). The reflections along the different *q*_z truncation rods are clearly defined at *T*_{sub} = 160 °C (Figure 2h), the highest temperature at which PDIF-CN₂ adsorbs on the native SiO_x surface under the applied experimental conditions. The fitted unit cell parameters listed in Table 1 (the corresponding best fit of the Bragg reflection positions is shown in Figure 2h as yellow stars) differ slightly from the reported single-crystal structure⁶⁷ and the Langmuir–Blodgett monolayer (ML).⁶⁸ Both PDIF-CN₂ and the RT-phase of PDIR-CN₂ exhibit an increase of the unit cell volume by ~10% in comparison with the reported structures, however, this might be caused by thermal expansion due to measurements at a high substrate temperature.

To investigate the stacking of the molecular layers in the out-of-plane direction, we performed XRR scans. The data presented in Figure 3 confirm the structural changes found upon increasing *T*_{sub}, as described above. The PDIR-CN₂ films

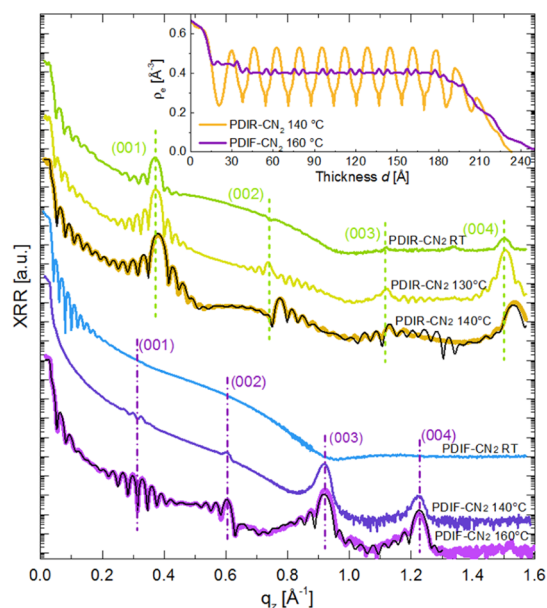


Figure 3. XRR profiles of PDIR-CN₂ and PDIF-CN₂ films grown at different *T*_{sub}. The black curves show fits for films with the highest crystallinity. The inset shows the electron density profiles obtained from the XRR fit. Vertical offset for clarity.

grown at a high *T*_{sub} reveal an enhanced crystallinity, which can be seen through the increased (001) and (004) Bragg peak intensity. The interlayer spacing *d*_z evaluated from the film grown at 140 °C (orange curve) does not deviate strongly from the RT-phase (Table 2). This might point toward a variation of

Table 2. Out-of-Plane Thin-Film Characteristics Extracted from XRR Profiles (See the Supporting Information)

	<i>d</i> , nm	σ_{XRR} , nm	σ_{AFM} , nm	<i>d</i> _z , Å	average inclination angle, ^a deg
PDIR-CN ₂ RT	21.6	1.5	1.0	16.75	44
PDIR-CN ₂ 130 °C	24.3	1.6	1.1 (120 °C)	16.73	32
PDIR-CN ₂ 140 °C	20.7	1.3	1.8	16.46	16
PDIF-CN ₂ RT	29.4	2.0	0.8		
PDIF-CN ₂ 140 °C	27.3	6.0	7.5	20.6	
PDIF-CN ₂ 160 °C	20.4	2.5	1.9	20.4	

^aHere, the inclination angle is the average angle between the long molecular axis and the surface. The approximate values are assumed using a single-molecule model (see the Supporting Information) and given to illustrate the general temperature dependence.

the unit cell predominantly along the *a*- and *b*-axis. More dramatic changes were observed for PDIF-CN₂ following the transition from the amorphous (RT) to the highly textured film [160 °C, (003) and (004) Bragg reflections being the most pronounced].

An interesting effect of strong suppression of some of the Bragg reflections is observed in both cases. To quantify how the molecular arrangement influences the reflectivity scans, we performed a fit of the reflectivity curves using GenX⁶⁹ (see the Supporting Information for more details). Because each molecule consists of a PDI core and two side chains, each ML in the model was divided into three sublayers, varying their relative electron density, thickness, and roughness. The resulting *z*-dependent electron density is shown in the inset (Figure 3), and the corresponding parameters are presented in Table 2. As seen from the fit, for PDIR-CN₂ the difference in the electron density between the core and the side chains is pronounced and enhanced by a tilted molecule orientation, whereas for the standing PDIF-CN₂ molecules, the electron density exhibits only weak modulations (see Figures S3–S7 and ref 70). The smaller values of the inclination angle in PDIR-CN₂ films grown at HT are consistent with the presence of a different crystal polymorph. As shown, ρ_e of the fluorinated chain is higher (0.420 Å⁻³) than ρ_e of the alkyl chain (0.312 Å⁻³) and that of the PDI backbone (0.405 Å⁻³) because of the higher atomic number of fluorine atoms.

In addition to information on the crystal structure, XRR is a precise method to determine the thickness and roughness. These parameters extracted from the width and depth of the Kiessig oscillations (i.e., the interference oscillations at low *q*_z) are shown in Table 2. All PDIR-CN₂ films exhibit a small surface roughness (σ does not exceed 2 nm), and no strong changes are observed upon the temperature increase. However, the roughness of the PDIF-CN₂ films change nonmonotonously with the substrate temperature. It changes from a very smooth film with ($\sigma \approx 2.0$ nm) to a much rougher surface ($\sigma \approx 6.0$ nm), and then, with the further temperature increase, the

film becomes smooth again ($\sigma \approx 2.5$ nm). For further investigations of this behavior and other surface properties, we refer to the discussion of the AFM images further below.

Optical Absorption Spectra. Optical properties of organic materials are strongly influenced by the molecular environment. The resulting spectroscopic signatures of thin films usually deviate significantly from the monomer spectra in solution because of intermolecular interactions.^{71–73} Two mechanisms for such interactions may be considered: (1) the excited-state resonance dipole–dipole interaction described for two ideal cases of the so-called J- and H-aggregations by Kasha et al.,⁷⁴ where different arrangements of strongly coupled, parallel, translated transition dipole moments are responsible for either a red-shifted or blue-shifted absorption due to exciton-state splitting and (2) nonresonant interactions causing a “gas-to-crystal” shift of energy levels because of changes of the polarizability of the molecular environment. Taking into account the optical anisotropy in materials that exhibit crystalline order, it is very useful to consider the optical features decoupled along different crystalline directions.⁷⁵ For this purpose, we applied variable angle spectroscopic ellipsometry, which allows to probe optical anisotropy in thin films.^{60,61}

The in-plane ($\epsilon_{2,xy}$) and out-of-plane ($\epsilon_{2,z}$) components of the dielectric function (i.e., parallel and perpendicular to the substrate plane, respectively) of different PDIR-CN₂ and PDIF-CN₂ thin films are shown in Figure 4 in comparison with the absorption spectra in solution. The spectral shape of $\epsilon_{2,xy}$ of PDIR-CN₂ films does not deviate strongly from that of the solution, although a significant red shift of about 200 meV is present. According to the extension of Kasha’s theory, taking exciton-vibrational coupling into account,^{76–78} an increase (decrease) of the oscillator strength of the 0–0 vibronic band

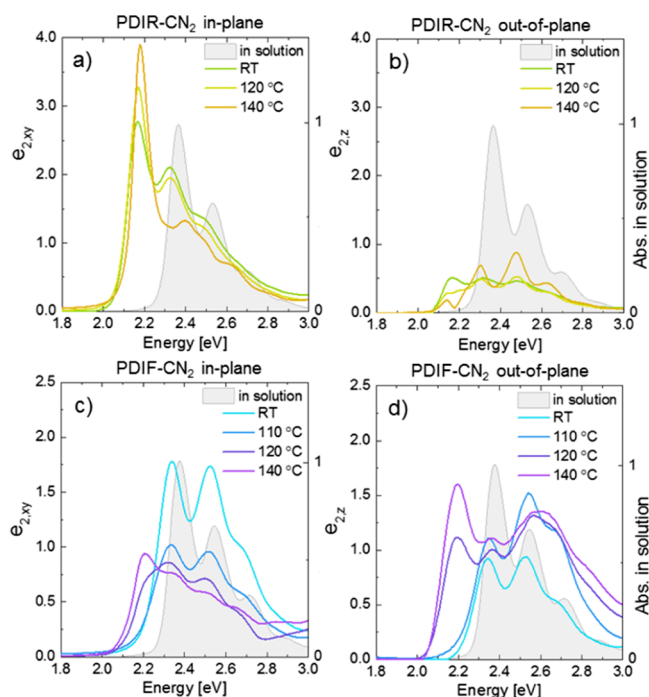


Figure 4. Dielectric function of the in-plane (a,c) and out-of-plane (b,d) components of thin films prepared at different T_{sub} in comparison with the absorption spectra in solution. Top: PDIR-CN₂; bottom: PDIF-CN₂.

compared to the 0–1 vibronic band along with the appearance of a low (high)-energy transition are strong signatures of enhanced J(H)-like coupling. An interesting observation is that the magnitude of the lowest transition I_{0-0} (at 2.18 eV) increases with T_{sub} as well as its ratio to the second vibronic peak (at 2.32–2.40 eV): I_{0-0}/I_{0-1} for the RT film is ~ 1.3 and increases up to ~ 3.0 in the 140 °C film.

Also, a substructure of the vibronic peaks in the 140 °C film (e.g., at 2.3 and 2.5 eV) shows up, giving a hint toward the presence of a second component. The out-of-plane component is much less intense, which is explained well by the highly tilted molecular orientation with a transition dipole moment μ mostly located in the xy -plane. Furthermore, the 0–0 out-of-plane transition undergoes a splitting appearing at $T_{\text{sub}} = 120$ °C, which becomes very pronounced at $T_{\text{sub}} = 140$ °C. This feature is possibly a Davydov splitting, keeping in mind the HT-phase with two molecules per unit cell as shown before. Both ϵ_2 spectra were fitted with Gaussians to confirm the presence of two Davydov components in the optical transitions. The fit is provided in Figure S9, Supporting Information. The temperature-dependent spectral changes are also consistent with the orientational changes toward more lying down molecules of the HT-phase (Table 2). Because of the Davydov splitting being an anisotropic effect sensitive to the intermolecular geometry^{72,75} and the transition dipole moment of PDI being oriented along the long molecular axis, the decrease of the inclination angle in PDIR-CN₂ at 140 °C film results in an intensity increase of the lowest transition (0–0), which belongs to the low energy Davydov component oriented in the in-plane direction.

PDIF-CN₂ thin films reveal a qualitatively different optical behavior (Figure 4c,d). The RT film exhibits a small red shift of only 40 meV compared to the solution spectrum and a similar shape for both anisotropic components, with the I_{0-0}/I_{0-1} ratio close to unity (whereas in solution, the ratio is ~ 1.5). The similarity with the spectrum in solution can be explained by the low crystallinity of the thin films, which leads to reduced intermolecular interaction and therefore to an optical response of the molecular aggregates similar to that of the single molecule. Nevertheless, the distortion of the Poissonian Franck–Condon vibronic progression determined in solution (Figures 1 and 4) evidences that a weak coupling is still present. As in the previous case of PDIR-CN₂, the horizontal component is also stronger here although the difference is not as dramatic (only 2-fold instead of 4-fold). This is consistent with the observation of a weak preferred in-plane orientation in the almost disordered film (Figure 2d). When growing at higher substrate temperatures, the absorption spectrum undergoes significant changes. First, the horizontal and vertical components swap their relative intensities as a consequence of the orientational change when going from a weakly ordered to a crystalline film where molecules stand upright relative to the substrate surface. At 110 °C, a blue shift of the absorption maximum for the out-of-plane direction toward 2.6 eV is observed. Moreover, a pronounced red-shifted transition around 2.2 eV similar to the one in PDIR-CN₂ emerges in both the in-plane and out-of-plane directions as T_{sub} is further increased. This coincides with the long-range crystal structure formation in PDIF-CN₂ thin films above 120 °C (Figure 2e–g).

Real-Time Study: GIXD and DRS. Next, we will discuss the structure formation and phase behavior at early growth stages, for which we monitored the crystalline structure evolution by GIXD scanning in situ and real time during film

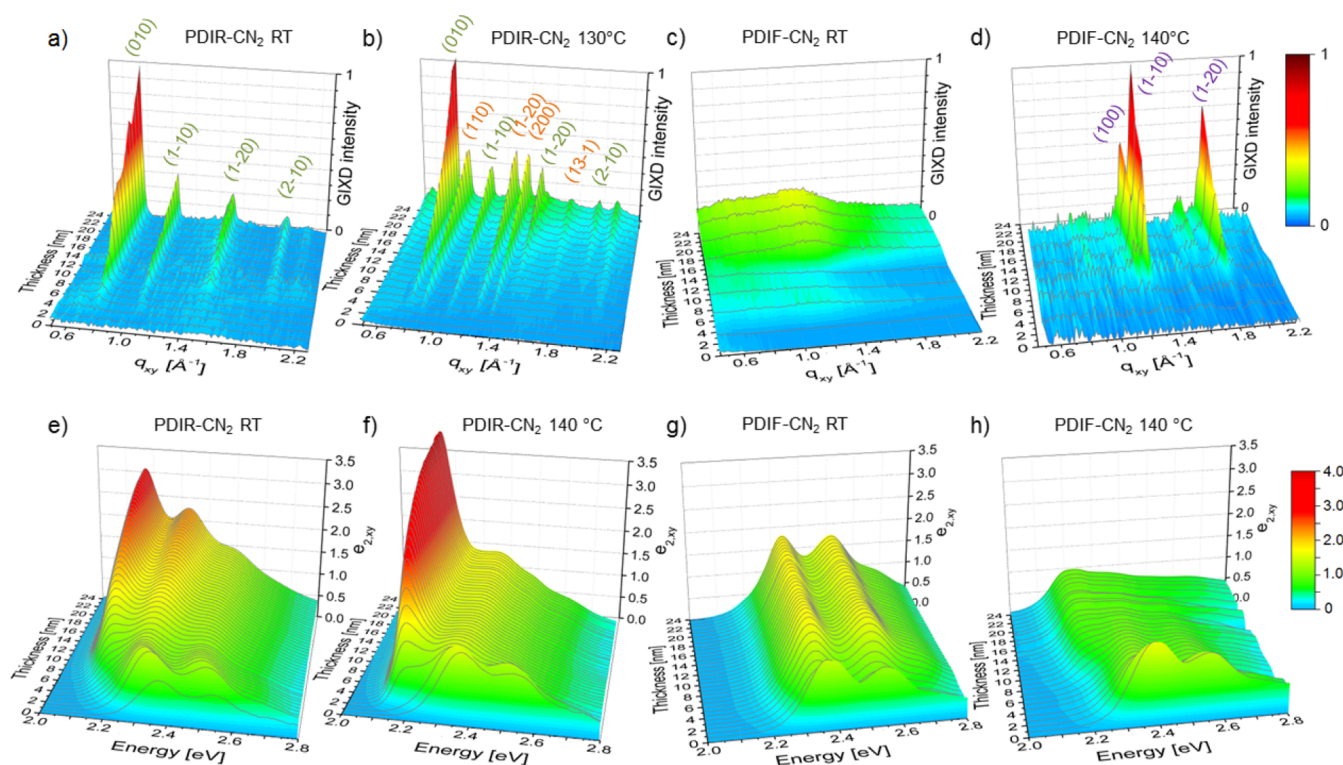


Figure 5. (a–d) Real-time GIXD plots. The vertical axis corresponds to the normalized intensity. The intensity of PDIF-CN₂ at RT in the absence of strong peaks is scaled relatively to PDIF-CN₂ at 140 °C. The Miller indices are shown for clarity only for the most pronounced peaks, but the intensities may include contribution of multiple reflections (see Figure 2); green labels stand for the RT-phase and orange labels for the HT-phase of PDIR-CN₂. (e–h) Dielectric function spectra determined by fitting the DRS data recorded during growth.

growth. The resulting film thickness dependences for both compounds grown at room and high substrate temperatures are plotted in Figure 5. The elevated temperatures of 130 and 140 °C were chosen to show the coexistence of both polymorphs in PDIR-CN₂ films and the crystalline phase in PDIF-CN₂ films. The observable q -range corresponds to a horizontal cut through the q -maps in Figure 2 at q_z close to zero.

The Bragg peaks in PDIR-CN₂ of the RT crystal phase appear after the first 4 nm at q_{xy} of 0.76 and 1.06 \AA^{-1} as the strongest features (Figure 5a). Taking into consideration the vertical lattice spacing d_z of 16.8 \AA , as deduced from XRR, this thickness corresponds to the formation of the third ML. At $T_{\text{sub}} = 130$ °C (Figure 5b), the structural features of both crystal phases arises simultaneously after 3 nm, that is, earlier than in the first case—when the two first MLs are completed. Disordered PDIF-CN₂ at RT exhibits only a weak scattering feature at $q_{xy} = 1.2$ \AA^{-1} (Figure 5c). In contrast to the relatively fast nucleation process of PDIR-CN₂, any signs of crystallization in PDIF-CN₂ at $T_{\text{sub}} = 140$ °C are not observed until a thickness of about 8 nm is reached (Figure 5d) corresponding to about 4 MLs, considering $d_z = 20.4$ \AA as deduced from XRR.

The diffraction peaks were fitted using Gaussian functions, from which the in-plane coherent crystal grain size l_s can be derived.⁷⁹ The evolution of l_s and the integrated peak intensity versus film thickness are shown in the Supporting Information (Figure S8).

The two compounds examined in this study have a similar chemical structure and exhibit almost identical absorption spectra in solution. However, in the condensed state, their optical responses vary dramatically not only from one compound to another but also between different intermolecular arrangements. To correlate the optical features with the

structural properties, we use DRS, which allows monitoring the development of the in-plane component of the absorption from the beginning of film formation with high time resolution (Figure 5e–h).^{57,80–82}

It is remarkable that in all presented cases, the spectral shape of the first ML (approximately 1.5–2 nm) is almost identical to the solution spectrum, that is, a noncoupling arrangement. Here, only a small red shift induced by the environment appears until the first ML is complete. Also a slight decrease of $\epsilon_{2,xy}$ after this thickness is observed. A new low-lying transition shows up at 2.2 eV in all crystalline films except for PDIF-CN₂ at RT, where the shape of the in-plane dielectric function remains unchanged because of the absence of long-range order in the film. The new absorption band at 2.2 eV appears after the first ML in PDIR-CN₂ at 140 °C and grows earlier in comparison with the RT film. Thickness intervals over which the peak intensity increases—from 5 to 16 nm and from 2 to 8 nm for the RT and HT films, respectively—coincide with the saturation times of the crystal grain sizes for these cases. These observations are in good agreement with the enhanced crystallinity of the HT film and confirm the intermolecular electronic coupling as a reason for such a behavior. This trend is delayed in PDIF-CN₂ (140 °C) as a consequence of the later structural stabilization because the diffraction peaks are observed at thicknesses above 8–10 nm. The comparison between evolutions of the crystal phases and the lowest electronic transition is provided in Figure S8, Supporting Information.

To better illustrate the variation of the dielectric function during the film growth, we implement an approach introduced by Ghanbari et al.,⁸³ who used an incremental change of the DRS signal as a function of time. Here, we use the difference

between the individual spectra of $e_{2,xy}$ obtained as a fit result from raw DRS data [two-dimensional (2D) images of the $\Delta e_{2,xy}$ in Figure 6a]. In a simplified view, three growth steps can be

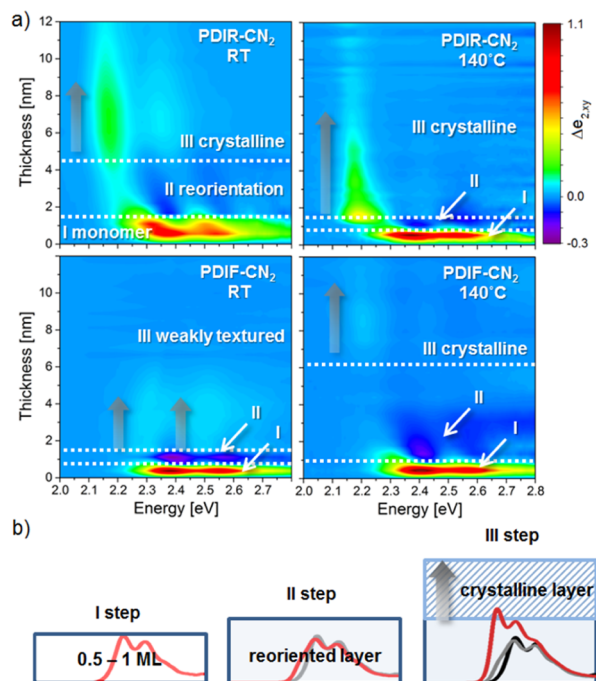


Figure 6. (a) $\Delta e_{2,xy}$ spectra based on the data set from Figure 5e–h revealing incremental changes in absorption at early growth stages. The gray arrows are a guide to the eye. (b) Sketch associating the spectral and structural changes in the films.

distinguished in each case, as sketched in Figure 6b. At first, the material absorbs randomly on the surface, and its absorption resembles the monomer spectra of almost noninteracting molecules. Then, after 0.5–1 ML, the deposited molecules start to interact with the newly arriving molecules, which leads to their reorientation to some extent.¹¹⁰ The reoriented layer serves as a precursor for a crystalline phase or, in the case of PDIF-CN₂ at RT, a weakly ordered phase with molecules tending to lie down. The evidence for transformation between the different spectral components is a reduction of the absorption (dark blue areas in Figure 6a) and the smooth red shift in the case of crystalline samples (with the exception of PDIF-CN₂ at RT) in step II. Therefore, the contribution to the resulting spectrum from the material of step I is no longer observed, whereas all spectra in step III present a combination of the reoriented and crystalline layers. The border between steps II and III is consistent with the thickness, after which the crystalline peaks are observed in real-time GIXD data.

The described phenomenon is in contrast to what we observed for highly crystalline, vertically aligned materials on SiO_x substrates such as DIP, PEN, perfluoropentacene, or PDI8-CN₂, where optical changes caused by the crystalline structure formation are observed within the first ML.^{47,82}

PL. PL spectroscopy is a highly sensitive technique to probe intermolecular interactions stemming from the arrangement in solid-state organic films.⁴⁶ In Figure 7 we compare temperature-dependent PL spectroscopy to the in-plane absorption. The films with a crystalline structure (i.e., PDIR-CN₂ grown at both RT and at 140 °C and PDIF-CN₂ grown at 140 °C) measured at a temperature of 20 °C (Figure 7a,b,d) reveal a

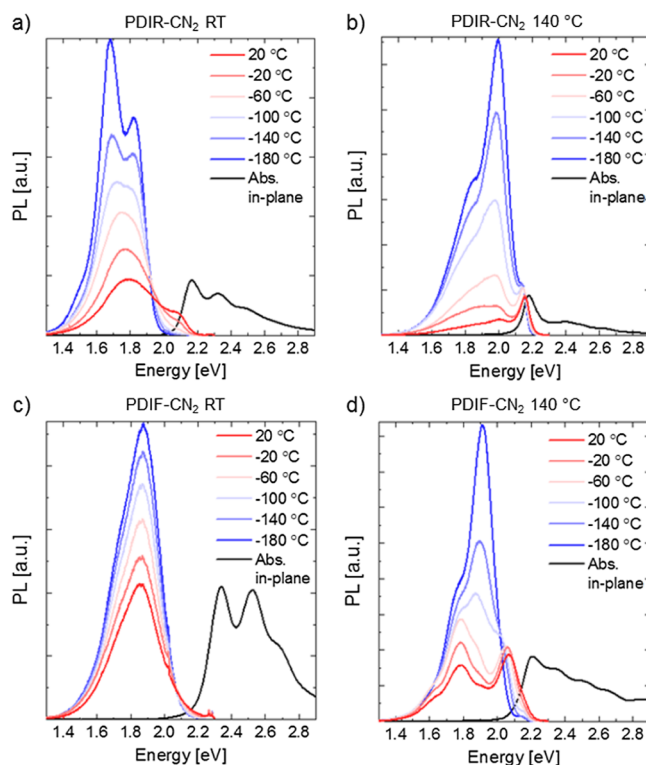


Figure 7. Temperature-dependent PL spectra recorded between 20 °C (red) and –180 °C (blue). Top: PDIR-CN₂ grown at RT (a) and at HT (b); bottom: PDIF-CN₂ grown at RT (c) and at HT (d). The black curves represent $e_{2,xy}$ from Figure 4 rescaled to the 20 °C curves.

nearly mirror-symmetric first band (at 2.08, 2.15, and 2.05 eV, respectively) caused by intermolecular coupling, as discussed above. Along with this observation, Stokes shifts appear to be smaller in the case of PDIR-CN₂, that is, 90 and 26 meV versus 143 meV in PDIF-CN₂. The efficiency of such radiative transitions caused by the intermolecular coupling is very sensitive to the degree of spatial separation such as a x -/ y -displacement or the tilt angle between molecules.^{74,84} This might explain why in the cases of the highly ordered films, the high-energy transitions are not distinguishable at low measurement temperatures, when contributions from breathing and shearing vibronic modes decay.⁸⁵ Then, the radiative recombination of the relaxed singlet excitons results in a strong rise of the emission with a resolved vibronic progression (a relaxed exciton) taking over below –100 °C. A similar behavior of two competing temperature-dependent contributions was observed for the PL spectra of 6T films.^{86,87} Also, the PDIF-CN₂ (140 °C) emission spectra contain a low-energy component at 1.78 eV visible while cooling down to –100 °C. In ref 37, this component was assigned to the long-lived excimer-like radiation, which often stands out as a characteristic feature of a cofacial overlap in π - π -stacks.⁴⁶

The singlet exciton emission band shape of the molecular crystal lattice is not observed in the PDIR-CN₂ and PDIF-CN₂ films grown at RT (Figure 7a,c). In PDIR-CN₂, a vibronically structured emission emerges at low temperatures as well as in HT-deposited films, however, the transitions are significantly red-shifted, and the spectral shape does not reveal the singlet exciton-like distributed vibronic peak intensities but a maximum around 1.69 eV. A possible explanation could be long-lived trap states.⁶¹ The PDIF-CN₂ film shows a uniform featureless red-shifted broad emission band over the whole

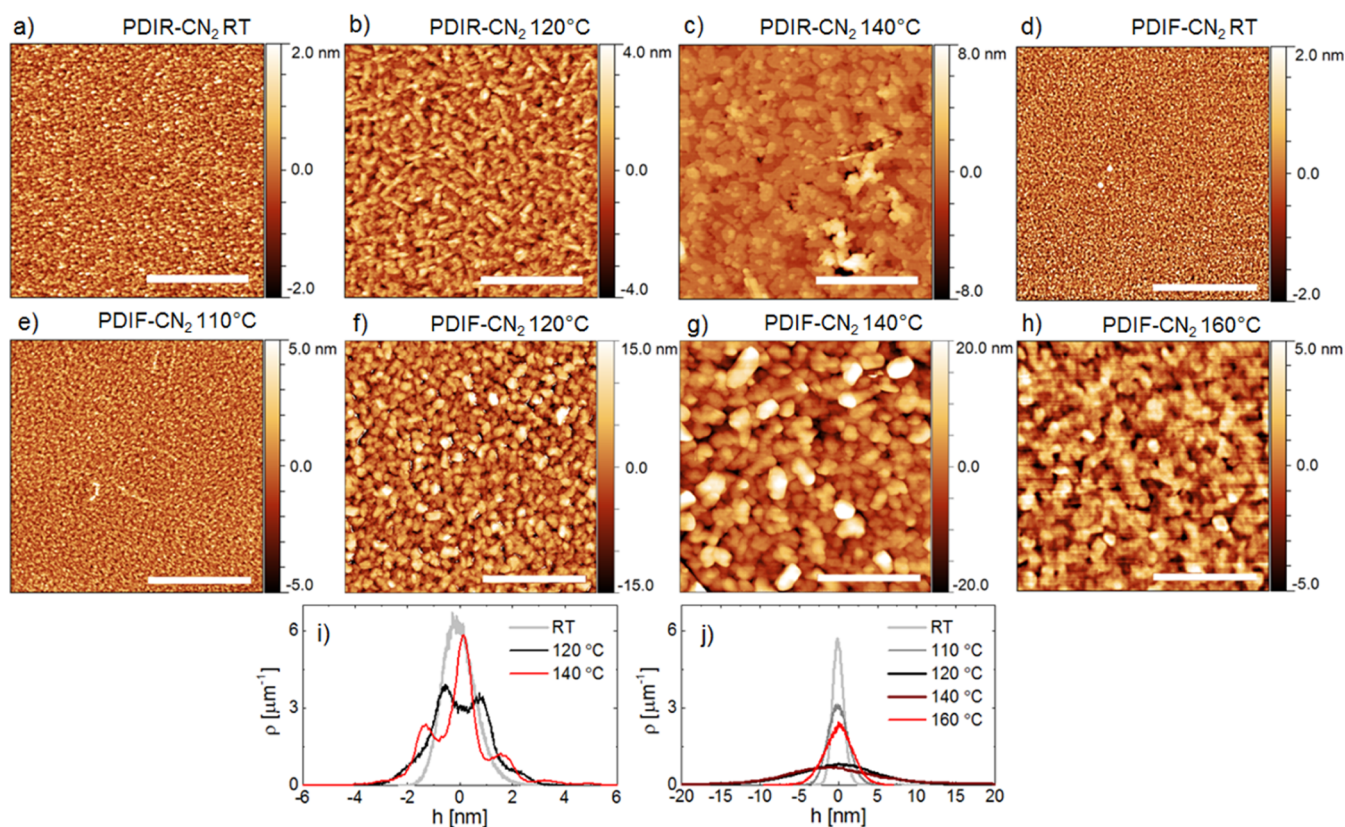


Figure 8. AFM images ($5 \times 5 \mu\text{m}$) of different PDIR-CN₂ films (a–c) and PDIF-CN₂ (d–h) with the corresponding height distributions (i) PDIR-CN₂ and (j) PDIF-CN₂. Length of the scale bar is $2 \mu\text{m}$.

measured temperature range, which is typical for the excimer emission observed for perylene derivatives.^{34,46,88,89} Although the excimer-like emission is usually ascribed to H-dimeric coupling in aggregates with an optimized face-to-face overlap, this recombination path is surprisingly effective in the only weakly ordered PDIF-CN₂ grown at RT. Nevertheless, as shown in numerous works on PDI dimers and trimers, the introduction of spacer groups indeed reduces the coupling strength, but does not fully suppress the excimer-like emission up to a center-to-center distance between two PDI subunits of $7\text{--}8 \text{ \AA}$.^{90–92}

Morphology. When designing organic electronic devices, special attention should be paid to the active layer morphology because of a direct correlation between domain extension and device electrical performance.^{6,32,35} The morphology of the samples was probed by AFM. The images together with the corresponding height distributions are shown in Figure 8. PDIR-CN₂ grown at RT exhibits a homogenous surface consisting of small grains and a high island density. The height variation around the average is $\pm 2 \text{ nm}$, and the root-mean-square roughness σ_{rms} is on average 1 nm . The morphology of PDIR-CN₂ thin films changes significantly when growing them on a heated substrate. At $T_{\text{sub}} = 120 \text{ }^\circ\text{C}$, the grain shape changes to elongated islands that exhibit distinct steps, revealing an anisotropic 2D growth inherent to other PDIs with alkyl chains.^{45,93} Wide flat terraces leading to a low roughness appear at a higher substrate temperature of $140 \text{ }^\circ\text{C}$, which is in good agreement with the low roughness determined by XRR. There are two explanations for the morphological differences between PDIR-CN₂ thin films grown at RT and at $140 \text{ }^\circ\text{C}$: (a) the enhanced diffusion at high substrate

temperatures⁹⁴ along with low Ehrlich–Schwöbel barriers promoting a relatively uniform coverage⁹⁵ and (b) the temperature-dependent polymorphism. As shown above, the HT thin film nucleates in a different crystal structure than the low-temperature film, and hence, depending on the crystal structure, different growth rates for lateral and vertical crystallographic directions may appear.^{93,96} The step heights between the plateaus derived from the height distribution are $1.5 \pm 0.5 \text{ nm}$, which is roughly the lattice spacing of a PDIR-CN₂ unit cell, which leads to the conclusion that each of the terraces consists of one layer of PDIR-CN₂ molecules. We note that a Stranski–Krastanov growth mode, that is, layer-plus-islands, is typical for PDIs.^{35,46,93,97}

The PDIF-CN₂ film grown at RT is the smoothest thin film of this series (σ_{rms} derived from the AFM images is below 1.0 nm). The missing crystalline ordering in PDIF-CN₂ thin films grown at RT may account for the low roughness. The molecules spread evenly over the substrate without forming clusters. The small grain morphology of PDIs was suggested to be rich in inhomogeneities and structural defects.³ A similar morphology is observed for PDIF-CN₂ at $110 \text{ }^\circ\text{C}$. A strong trend to roughening can be seen when growing at 120 and $140 \text{ }^\circ\text{C}$. Large 3D clusters with σ_{rms} of several nanometers form. The deviations from the average height reach up to ± 15 and 20 nm in each case. The crystallization at high T_{sub} presumably drives the formation of larger clusters. The growth rate along the crystallographic direction perpendicular to the substrate surface has to be increased compared to the rate of PDIR-CN₂. It was shown how the introduction of substitutions with different degrees of steric hindrance and introduction of fluorine atoms increase both surface diffusion and step-edge

diffusion barriers.^{98–100} However, going to the highest growth temperature of 160 °C, the roughness decreases again because of the formation of flatter domains, which is in good agreement with the XRR data. At this growth temperature, the enhanced diffusivity seems to efficiently balance the Ehrlich–Schwöbel barrier at the step edges of the crystalline molecular layers. Under these conditions, highly crystalline and smooth films can be obtained.

To summarize, for both compounds, we can see a clear transition in the nucleation behavior, which coincides with changes in the crystal structure. We have shown that the continuous morphology with a minimized number of grain boundaries, the most beneficial situation for high charge mobility,^{32,48,101} can be achieved via the substrate temperature control.

DISCUSSION

As pointed out in the introduction, the electronic structure of the perylene derivatives is considered to be not strongly affected by substituents in the imide positions in their single-molecule state. However, all parameters that are crucial for device performance, that is, the charge-transport properties, energy structure, photon absorption and emission, morphological organization, crystalline quality, and so forth are based on the growth behavior, which strongly depends on interactions of the monomer with the environment. The behavior of the compounds considered here contrasts to compounds with linear alkyl chains such as PTCDI-C₈⁹³ and PDI8-CN₂,⁴⁶ which grow in nearly upright standing fashion starting from the first ML on SiO_x substrates. Despite the fact that partial fluorination is often considered to introduce a strong noncovalent stabilizing interaction,^{17,18,102,103} we note here that PDIF-CN₂ generally reveals less tendency for crystallization than non-fluorinated compounds, such as PDIR-CN₂ and PDI8-CN₂. Although the branched and fluorinated side chains break the molecule's planarity in both cases,⁴⁰ for the same deposition conditions, PDIF-CN₂ requires a higher thermal energy to achieve the energetically favorable orientation in the lattice. The same crystallization-obstructing effect was observed for perfluorinated cobalt phthalocyanine F₁₆CoPc¹⁰⁴ and in the more relevant family of diperfluorohexylthiophenes DFH-*n*Ts, rod-like molecules with -C₆F₁₃ chains, which crystallize upon deposition at a substrate temperature of 120–200 °C into a similar packing motif.¹² One is tempted to conclude that this is a general trend for compounds containing fluoroalkyl chains. The reason for this might be in the bulkiness and the larger van der Waals radius of fluorine atoms compared to hydrogen limiting the fluoroalkyl chain's flexibility.^{43,105} A reasonable argument explaining the reduced contrast in the fitted electron density profile perpendicular to the substrate plane (Figure 3, inset) is that the high electron density of the fluorinated chains can shield the PDI backbones inhibiting the π - π intermolecular coupling. Interestingly, the structural transition to the long-range order occurs sharply almost in a step-like manner upon an increase of T_{sub} , which was observed by changes in the structural, morphological, and optical properties. In this context, one should bear in mind the difference between fluoroalkyl substituents and (complete/partial) fluorination of a molecular aromatic core when considering the fluorination effects.

The increase of thermal energy (substrate temperature) gives rise to structural changes in PDIR-CN₂ thin films, leading to the appearance of a HT-polymorph with two molecules per

unit cell. The RT-phase consists of molecules tilted toward a substrate nested together in a 1D slipped π - π -stacking with an offset along the long molecular axis (Figure 9a) due to shape

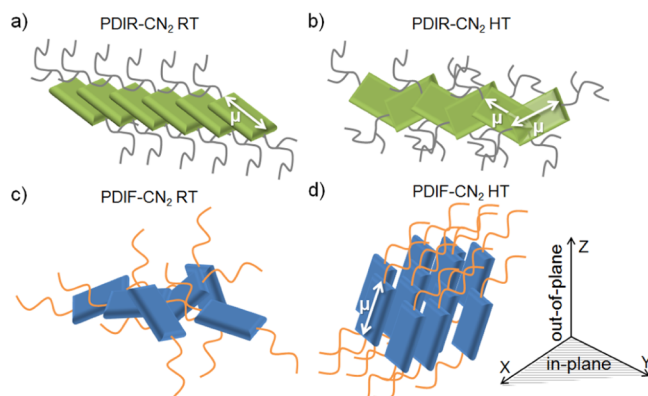


Figure 9. Schematics representing molecular arrangement in (a) PDIR-CN₂ RT-phase, (b) PDIR-CN₂ HT-phase, (c) amorphous PDIF-CN₂, and (d) PDIF-CN₂ thin-film crystal phase.

complementarity. This is a beneficial arrangement for J-like coupling, although common PDI derivatives in the absence of spatial crowding tend to create an ideal face-to-face conformation in columnar stacks with the typical properties of H-aggregation. Indeed, we observed a red-shifted 0–0 transition growing coherently with the crystal phase formation. When the HT-phase appears in a film (starting from $T_{\text{sub}} = 120$ °C), the J-aggregation character enhances significantly: the intensity of 0–0 grows not only in the absolute value but also relative to the next 0–1 transition. The anisotropic Davydov splitting observed in both the in-plane and out-of-plane directions indicates twisting of the transition dipole moments of two molecules contained in the unit cell, as illustrated in Figure 9b, similar to that described by Austin et al.⁷⁵ The change from 1D elongated island growth of the RT-phase rich film to the isotropic 2D flat terrace growth of the HT-phase rich film observed with AFM could be caused by a change in the crystal growth directions. A rotational offset configuration was found to be the third and deepest minimum of the binding energy in DFT calculations⁴⁴ and is widespread in PDI solution-processed supramolecular stacks^{27,44} but rather rare in crystals.^{75,106} Structural polymorphism upon vacuum deposition was also described for the parent perylene molecule,³⁴ however, for the related compound PDI8-CN₂ with linear chains, persistence of the same crystalline structure for a wide temperature range was observed.¹⁰⁷

The crystal phase of PDIF-CN₂ is arranged in a different way. Similar to many other perylene derivatives with chains in the imide position, it grows in a standing upright manner (in contrast with the disordered RT films where a majority of molecules tend to lie down, Figure 9c) but with a more complicated interlayer organization. Despite the contribution of -C₇F₁₄ chains, the typical π - π intermolecular PDI core interaction is still dominant, promoting a face-to-face configuration. Yet, the parallel stacking involves longitudinal and transverse offsets, that is, along both the long and short molecular axes, creating a 2D brick-wall-like pattern (Figure 9d). Such a 2D π - π -stack packing motif has been suggested as more favorable in terms of electronic coupling and charge percolation pathways.³³ For such complicated structures, the ideal classical cases of J-/H-aggregation are not straightforward

to apply because the optical spectra (absorption and emission) contain characteristic features from both types. Similar cases were observed earlier, where it has been concluded that both kinds of couplings might be present at the same time. Their strength would depend then on the spatial separation in the corresponding directions.¹⁰⁸ Also, the energies of low- and high-energy vibronic bands can be pushed down and up by the coupling of Frenkel excitons with intermolecular charge-transfer states and Coulombic interaction, respectively.^{71,72,75,109}

CONCLUSIONS

In summary, we followed the growth process of two PDI derivatives during vacuum deposition as a function of the substrate temperature. At the first ML, we find almost identical nonaggregating states without long-range order because of a shielding effect of the side substituents, which is stronger in the case of the fluorinated chains. This is followed by a temperature-dependent transition to significantly different crystalline molecular packing motifs influenced by the geometry and chemical composition of the side chains. This results in unique optical and structural properties, in sharp contrast to both the amorphous and the monomer properties, which are not affected by the chemical modification of the side substituents, as predicted by the previous DFT studies. The results are not only helpful for the future engineering of well-performing organic n-type active layers with desirable characteristics but also contribute to a fundamental understanding of condensed-state properties of organic small-molecule semiconductor materials.

ASSOCIATED CONTENT

Supporting Information

The Supporting Information is available free of charge on the ACS Publications website at DOI: 10.1021/acs.jpcc.8b00787.

GIXD scans of PDIR-CN₂ films, *q*-map of the PDIF-CN₂ RT film, electron density fits for all samples, additional details on the real-time analysis, and decomposition of the optical spectra of PDIR-CN₂ (PDF)

AUTHOR INFORMATION

Corresponding Authors

*E-mail: valentina.belova@uni-tuebingen.de (V.B.).

*E-mail: alexander.hinderhofer@uni-tuebingen.de (A.H.).

ORCID

Valentina Belova: 0000-0002-8142-2090

Alexander Hinderhofer: 0000-0001-8152-6386

Author Contributions

The manuscript was written through contributions of all authors. All authors have given approval to the final version of the manuscript.

Notes

The authors declare no competing financial interest.

ACKNOWLEDGMENTS

This work was supported by the Deutsche Forschungsgemeinschaft (SCHR 700/20–1). We are grateful for the provided beamtimes at the beamline ID10 of the European Synchrotron Radiation Facility (ESRF), Grenoble, France, and beamtime at MS-Surf-Diffr X04SA of the Swiss Light Source (SLS), Villigen, Switzerland. We thank Andrey Chumakov (ESRF) and Philip

Willmott (SLS) for the support during the synchrotron experiments. We thank Paul Beyer and Andreas Opitz, Humboldt-Universität zu Berlin und Marcus Scheele, Universität Tübingen for fruitful discussions. J. N. and J. R. acknowledge the support from the project CEITEC 2020 (grant no. LQ1601 financed by the MEYS of the Czech Republic). G.D. acknowledges the Carl Zeiss Stiftung. We also acknowledge support from DAAD/AWTR/MEYS grant no. 57215815/7AMB16DE006.

REFERENCES

- (1) Witte, G.; Wöll, C. Molecular Beam Deposition and Characterization of Thin Organic Films on Metals for Applications in Organic Electronics. *Phys. Status Solidi A* **2008**, *205*, 497–510.
- (2) Ringk, A.; Roelofs, W. S. C.; Smits, E. C. P.; van der Marel, V.; Salzmann, I.; Neuhold, A.; Gelinck, G. H.; Resel, R.; de Leeuw, D. M.; Strohrriegel, P. n-Type Self-Assembled Monolayer Field-Effect Transistors for Flexible Organic Electronics. *Org. Electron.* **2013**, *14*, 1297–1304.
- (3) Liscio, F.; Albonetti, C.; Broch, K.; Shehu, A.; Quiroga, S. D.; Ferlauto, L.; Frank, C.; Kowarik, S.; Nervo, R.; Gerlach, A.; et al. Molecular Reorganization in Organic Field-Effect Transistors and Its Effect on Two-Dimensional Charge Transport Pathways. *ACS Nano* **2013**, *7*, 1257–1264.
- (4) Anthony, J. E. Small-Molecule, Nonfullerene Acceptors for Polymer Bulk Heterojunction Organic Photovoltaics. *Chem. Mater.* **2011**, *23*, 583–590.
- (5) Hörmann, U.; Lorch, C.; Hinderhofer, A.; Gerlach, A.; Gruber, M.; Kraus, J.; Sykora, B.; Grob, S.; Linderl, T.; Wilke, A.; et al. *V_{oc}* from a Morphology Point of View: the Influence of Molecular Orientation on the Open Circuit Voltage of Organic Planar Heterojunction Solar Cells. *J. Phys. Chem. C* **2014**, *118*, 26462–26470.
- (6) Wilke, A.; Endres, J.; Hörmann, U.; Niederhausen, J.; Schlesinger, R.; Frisch, J.; Amsalem, P.; Wagner, J.; Gruber, M.; Opitz, A.; et al. Correlation between Interface Energetics and Open Circuit Voltage in Organic Photovoltaic Cells. *Appl. Phys. Lett.* **2012**, *101*, 233301.
- (7) Friend, R. H.; Gymer, R. W.; Holmes, A. B.; Burroughes, J. H.; Marks, R. N.; Taliani, C.; Bradley, D. D. C.; Santos, D. A. D.; Brédas, J. L.; Lögdlund, M.; et al. Electroluminescence in Conjugated Polymers. *Nature* **1999**, *397*, 121–128.
- (8) Heidenhain, S. B.; Sakamoto, Y.; Suzuki, T.; Miura, A.; Fujikawa, H.; Mori, T.; Tokito, S.; Taga, Y. Perfluorinated Oligo(p-Phenylene)s: Efficient n-Type Semiconductors for Organic Light-Emitting Diodes. *J. Am. Chem. Soc.* **2000**, *122*, 10240–10241.
- (9) Yamaguchi, Y. Effects of Fluorination on Electronic and Excited States of Fused Zinc Oligoporphyrins. *J. Chem. Phys.* **2005**, *122*, 184702.
- (10) Babudri, F.; Farinola, G. M.; Naso, F.; Ragni, R. Fluorinated Organic Materials for Electronic and Optoelectronic Applications: the Role of the Fluorine Atom. *Chem. Commun.* **2007**, 1003–1022.
- (11) Reddy, J. S.; Kale, T.; Balaji, G.; Chandrasekaran, A.; Thayumanavan, S. Cyclopentadithiophene-Based Organic Semiconductors: Effect of Fluorinated Substituents on Electrochemical and Charge Transport Properties. *J. Phys. Chem. Lett.* **2011**, *2*, 648–654.
- (12) Facchetti, A.; Mushrush, M.; Katz, H. E.; Marks, T. J. n-Type Building Blocks for Organic Electronics: A Homologous Family of Fluorocarbon-Substituted Thiophene Oligomers with High Carrier Mobility. *Adv. Mater.* **2003**, *15*, 33–38.
- (13) Sakamoto, Y.; Suzuki, T.; Kobayashi, M.; Gao, Y.; Fukai, Y.; Inoue, Y.; Sato, F.; Tokito, S. Perfluoropentacene: High-Performance p–n Junctions and Complementary Circuits with Pentacene. *J. Am. Chem. Soc.* **2004**, *126*, 8138–8140.
- (14) Subramanian, S.; Park, S. K.; Parkin, S. R.; Podzorov, V.; Jackson, T. N.; Anthony, J. E. Chromophore Fluorination Enhances Crystallization and Stability of Soluble Anthradithiophene Semiconductors. *J. Am. Chem. Soc.* **2008**, *130*, 2706–2707.
- (15) Uttiya, S.; Raimondo, L.; Campione, M.; Miozzo, L.; Yassar, A.; Moret, M.; Fumagalli, E.; Borghesi, A.; Sassella, A. Stability to Photo-

Oxidation of Rubrene and Fluorine-Substituted Rubrene. *Synth. Met.* **2012**, *161*, 2603–2606.

(16) Anger, F.; Breuer, T.; Ruff, A.; Klues, M.; Gerlach, A.; Scholz, R.; Ludwigs, S.; Witte, G.; Schreiber, F. Enhanced Stability of Rubrene against Oxidation by Partial and Complete Fluorination. *J. Phys. Chem. C* **2016**, *120*, 5515–5522.

(17) Ponzini, F.; Zagha, R.; Hardcastle, K.; Siegel, J. S. Phenyl/Pentafluorophenyl Interactions and the Generation of Ordered Mixed Crystals: sym-Triphenethynylbenzene and sym-Tris-(perfluorophenethynyl)benzene. *Angew. Chem.* **2000**, *112*, 2413–2415.

(18) Collings, J. C.; Roscoe, K. P.; Thomas, R. L.; Batsanov, A. S.; Stimson, L. M.; Howard, J. A. K.; Marder, T. B. Arene-Perfluoroarene Interactions in Crystal Engineering. Part 3. Single-Crystal Structures of 1:1 Complexes of Octafluoronaphthalene with Fused-Ring Polyaromatic Hydrocarbons. *New J. Chem.* **2001**, *25*, 1410–1417.

(19) Fourmigué, M.; Batail, P. Activation of Hydrogen- and Halogen-Bonding Interactions in Tetrathiafulvalene-Based Crystalline Molecular Conductors. *Chem. Rev.* **2004**, *104*, 5379–5418.

(20) Taylor, R. It Isn't, It Is: The C–H···X (X = O, N, F, Cl) Interaction Really Is Significant in Crystal Packing. *Cryst. Growth Des.* **2016**, *16*, 4165–4168.

(21) Williams, J. H. The Molecular Electric Quadrupole Moment and Solid-State Architecture. *Acc. Chem. Res.* **1993**, *26*, 593–598.

(22) Nangia, A. Supramolecular Chemistry and Crystal Engineering. *J. Chem. Sci.* **2010**, *122*, 295–310.

(23) Ogden, W. A.; Ghosh, S.; Bruzek, M. J.; McGarry, K. A.; Balhorn, L.; Young, V., Jr.; Purvis, L. J.; Wegwerth, S. E.; Zhang, Z.; Serratore, N. A.; et al. Partial Fluorination as a Strategy for Crystal Engineering of Rubrene Derivatives. *Cryst. Growth Des.* **2017**, *17*, 643–658.

(24) Milián-Medina, B.; Gierschner, J. “Though It Be but Little, It Is Fierce”: Excited State Engineering of Conjugated Organic Materials by Fluorination. *J. Phys. Chem. Lett.* **2017**, *8*, 91–101.

(25) Dou, J.-H.; Zheng, Y.-Q.; Yao, Z.-F.; Yu, Z.-A.; Lei, T.; Shen, X.; Luo, X.-Y.; Sun, J.; Zhang, S.-D.; Ding, Y.-F.; et al. Fine-Tuning of Crystal Packing and Charge Transport Properties of BDOPV Derivatives through Fluorine Substitution. *J. Am. Chem. Soc.* **2015**, *137*, 15947–15956.

(26) Shao, Y.; Yin, G.-Z.; Ren, X.; Zhang, X.; Wang, J.; Guo, K.; Li, X.; Wesdemiotis, C.; Zhang, W.-B.; Yang, S.; et al. Engineering π – π Interactions for Enhanced Photoluminescent Properties: Unique Discrete Dimeric Packing of Perylene Diimides. *RSC Adv.* **2017**, *7*, 6530–6537.

(27) Ghosh, S.; Li, X.-Q.; Stepanenko, V.; Würthner, F. Control of H- and J-Type π Stacking by Peripheral Alkyl Chains and Self-Sorting Phenomena in Perylene Bisimide Homo- and Heteroaggregates. *Chem.—Eur. J.* **2008**, *14*, 11343–11357.

(28) Balakrishnan, K.; Datar, A.; Naddo, T.; Huang, J.; Oitker, R.; Yen, M.; Zhao, J.; Zang, L. Effect of Side-Chain Substituents on Self-Assembly of Perylene Diimide Molecules: Morphology Control. *J. Am. Chem. Soc.* **2006**, *128*, 7390–7398.

(29) Vijayalakshmi, S.; Föhlisch, A.; Kirchmann, P. S.; Hennies, F.; Pietzsch, A.; Nagasono, M.; Wurth, W. Bond Polarization and Image-Potential Screening in Adsorbed C₆F₆ on Cu(111). *Surf. Sci.* **2006**, *600*, 4972–4977.

(30) Wong, S. L.; Huang, H.; Huang, Y. L.; Wang, Y. Z.; Gao, X. Y.; Suzuki, T.; Chen, W.; Wee, A. T. S. Effect of Fluorination on the Molecular Packing of Perfluoropentacene and Pentacene Ultrathin Films on Ag (111). *J. Phys. Chem. C* **2010**, *114*, 9356–9361.

(31) Jiang, H.; Hu, P.; Ye, J.; Li, Y.; Li, H.; Zhang, X.; Li, R.; Dong, H.; Hu, W.; Kloc, C. Molecular Crystal Engineering: Tuning Organic Semiconductor from p-type to n-type by Adjusting Their Substitutional Symmetry. *Adv. Mater.* **2017**, *29*, 1605053.

(32) Lunt, R. R.; Benziger, J. B.; Forrest, S. R. Relationship between Crystalline Order and Exciton Diffusion Length in Molecular Organic Semiconductors. *Adv. Mater.* **2010**, *22*, 1233–1236.

(33) Geng, Y.; Li, H.-B.; Wu, S.-X.; Su, Z.-M. The Interplay of Intermolecular Interactions, Packing Motifs and Electron Transport

Properties in Perylene Diimide Related Materials: a Theoretical Perspective. *J. Mater. Chem.* **2012**, *22*, 20840–20851.

(34) Pick, A.; Klues, M.; Rinn, A.; Harms, K.; Chatterjee, S.; Witte, G. Polymorph-Selective Preparation and Structural Characterization of Perylene Single Crystals. *Cryst. Growth Des.* **2015**, *15*, 5495–5504.

(35) Vasseur, K.; Rolin, C.; Vandezande, S.; Temst, K.; Froyen, L.; Heremans, P. A Growth and Morphology Study of Organic Vapor Phase Deposited Perylene Diimide Thin Films for Transistor Applications. *J. Phys. Chem. C* **2010**, *114*, 2730–2737.

(36) Puigdollers, J.; Della Pirriera, M.; Marsal, A.; Orpella, A.; Cheylan, S.; Voz, C.; Alcubilla, R. N-type PTCDI–C₁₃H₂₇ Thin-Film Transistors Deposited at Different Substrate Temperature. *Thin Solid Films* **2009**, *517*, 6271–6274.

(37) Piliago, C.; Cordella, F.; Jarzab, D.; Lu, S.; Chen, Z.; Facchetti, A.; Loi, M. A. Functionalized Perylenes: Origin of the Enhanced Electrical Performances. *Appl. Phys. A* **2009**, *95*, 303–308.

(38) Kim, J.-H.; Han, S.; Jeong, H.; Jang, H.; Baek, S.; Hu, J.; Lee, M.; Choi, B.; Lee, H. S. Thermal Gradient During Vacuum-Deposition Dramatically Enhances Charge Transport in Organic Semiconductors: Toward High-Performance N-Type Organic Field-Effect Transistors. *ACS Appl. Mater. Interfaces* **2017**, *9*, 9910–9917.

(39) Wu, C.-H.; Chueh, C.-C.; Xi, Y.-Y.; Zhong, H.-L.; Gao, G.-P.; Wang, Z.-H.; Pozzo, L. D.; Wen, T.-C.; Jen, A. K.-Y. Influence of Molecular Geometry of Perylene Diimide Dimers and Polymers on Bulk Heterojunction Morphology toward High-Performance Non-fullerene Polymer Solar Cells. *Adv. Funct. Mater.* **2015**, *25*, 5326–5332.

(40) Sun, J.-P.; Hendsbee, A. D.; Dobson, A. J.; Welch, G. C.; Hill, I. G. Perylene Diimide Based All Small-Molecule Organic Solar Cells: Impact of Branched-Alkyl Side Chains on Solubility, Photophysics, Self-Assembly, and Photovoltaic Parameters. *Org. Electron.* **2016**, *35*, 151–157.

(41) Huang, C.; Barlow, S.; Marder, S. R. Perylene-3,4,9,10-tetracarboxylic Acid Diimides: Synthesis, Physical Properties, and Use in Organic Electronics. *J. Org. Chem.* **2011**, *76*, 2386–2407.

(42) Li, C.; Wonneberger, H. Perylene Imides for Organic Photovoltaics: Yesterday, Today, and Tomorrow. *Adv. Mater.* **2012**, *24*, 613–636.

(43) Jones, B. A.; Facchetti, A.; Wasielewski, M. R.; Marks, T. J. Tuning Orbital Energetics in Arylene Diimide Semiconductors. Materials Design for Ambient Stability of n-Type Charge Transport. *J. Am. Chem. Soc.* **2007**, *129*, 15259–15278.

(44) Würthner, F.; Saha-Möller, C. R.; Fimmel, B.; Ogi, S.; Leowanawat, P.; Schmidt, D. Perylene Bisimide Dye Assemblies as Archetype Functional Supramolecular Materials. *Chem. Rev.* **2016**, *116*, 962–1052.

(45) Liscio, F.; Milita, S.; Albonetti, C.; D'Angelo, P.; Guagliardi, A.; Masciocchi, N.; Della Valle, R. G.; Venuti, E.; Brillante, A.; Biscarini, F. Structure and Morphology of PDI8-CN₂ for n-type Thin-Film Transistors. *Adv. Funct. Mater.* **2012**, *22*, 943–953.

(46) Brillante, A.; Salzillo, T.; Della Valle, R. G.; Venuti, E.; Borgatti, F.; Lunedei, E.; Liscio, F.; Milita, S.; Albonetti, C. Photoluminescence as a Probe of Molecular Organization in PDI8-CN₂ Ultra-Thin Films. *J. Lumin.* **2017**, *187*, 403–409.

(47) Keil, C.; Graaf, H.; Baumgärtel, T.; Trenkmann, I.; Schlettwein, D. Intralayer vs. Interlayer Electronic Coupling in Perylene Imide Thin Films. *Org. Electron.* **2013**, *14*, 2833–2839.

(48) Jones, B. A.; Facchetti, A.; Wasielewski, M. R.; Marks, T. J. Effects of Arylene Diimide Thin Film Growth Conditions on n-Channel OFET Performance. *Adv. Funct. Mater.* **2008**, *18*, 1329–1339.

(49) Chiarella, F.; Barra, M.; Ricciotti, L.; Aloisio, A.; Cassinese, A. Morphology, Electrical Performance and Potentiometry of PDIF-CN₂ Thin-Film Transistors on HMDS-Treated and Bare Silicon Dioxide. *Electronics* **2014**, *3*, 76–86.

(50) Sakamoto, Y.; Komatsu, S.; Suzuki, T. Tetradecafluorosextiophene: The First Perfluorinated Oligothiophene. *J. Am. Chem. Soc.* **2001**, *123*, 4643–4644.

(51) Hinderhofer, A.; Heinemeyer, U.; Gerlach, A.; Kowarik, S.; Jacobs, R. M. J.; Sakamoto, Y.; Suzuki, T.; Schreiber, F. Optical

Properties of Pentacene and Perfluoropentacene Thin Films. *J. Chem. Phys.* **2007**, *127*, 194705.

(52) Peisert, H.; Knupfer, M.; Schwieger, T.; Fuentes, G. G.; Olligs, D.; Fink, J.; Schmidt, T. Fluorination of Copper Phthalocyanines: Electronic Structure and Interface Properties. *J. Appl. Phys.* **2003**, *93*, 9683–9692.

(53) Heimele, G.; Salzmänn, I.; Duhm, S.; Koch, N. Design of Organic Semiconductors from Molecular Electrostatics. *Chem. Mater.* **2011**, *23*, 359–377.

(54) Watanabe, T.; Hosokai, T.; Koganezawa, T.; Yoshimoto, N. In Situ Real-Time X-Ray Diffraction During Thin Film Growth of Pentacene. *Mol. Cryst. Liq. Cryst.* **2012**, *566*, 18–21.

(55) Kowarik, S.; Gerlach, A.; Sellner, S.; Schreiber, F.; Cavalcanti, L.; Konovalov, O. Real-Time Observation of Structural and Orientational Transitions during Growth of Organic Thin Films. *Phys. Rev. Lett.* **2006**, *96*, 125504.

(56) Lorch, C.; Banerjee, R.; Frank, C.; Dieterle, J.; Hinderhofer, A.; Gerlach, A.; Schreiber, F. Growth of Competing Crystal Phases of α -Sexithiophene Studied by Real-Time in Situ X-ray Scattering. *J. Phys. Chem. C* **2015**, *119*, 819–825.

(57) Hosokai, T.; Gerlach, A.; Hinderhofer, A.; Frank, C.; Ligorio, G.; Heinemeyer, U.; Vorobiev, A.; Schreiber, F. Simultaneous *in situ* Measurements of X-Ray Reflectivity and Optical Spectroscopy During Organic Semiconductor Thin Film Growth. *Appl. Phys. Lett.* **2010**, *97*, 063301.

(58) Schreiber, F. Organic Molecular Beam Deposition: Growth Studies Beyond the First Monolayer. *Phys. Status Solidi* **2004**, *201*, 1037–1054.

(59) Ritley, K. A.; Krause, B.; Schreiber, F.; Dosch, H. A Portable Ultrahigh Vacuum Organic Molecular Beam Deposition System for *in situ* X-Ray Diffraction Measurements. *Rev. Sci. Instrum.* **2001**, *72*, 1453–1457.

(60) Alonso, M. I.; Garriga, M.; Karl, N.; Ossó, J. O.; Schreiber, F. Anisotropic Optical Properties of Single Crystalline PTCDA Studied by Spectroscopic Ellipsometry. *Org. Electron.* **2002**, *3*, 23–31.

(61) Belova, V.; Beyer, P.; Meister, E.; Linderl, T.; Halbich, M.-U.; Gerhard, M.; Schmidt, S.; Zechel, T.; Meisel, T.; Generalov, A. V.; et al. Evidence for Anisotropic Electronic Coupling of Charge Transfer States in Weakly Interacting Organic Semiconductor Mixtures. *J. Am. Chem. Soc.* **2017**, *139*, 8474–8486.

(62) Herbst, S.; Soberats, B.; Leowanawat, P.; Lehmann, M.; Würthner, F. A Columnar Liquid-Crystal Phase Formed by Hydrogen-Bonded Perylene Bisimide J-Aggregates. *Angew. Chem., Int. Ed.* **2017**, *56*, 2162–2165.

(63) Chen, S.; Slattum, P.; Wang, C.; Zang, L. Self-Assembly of Perylene Imide Molecules into 1D Nanostructures: Methods, Morphologies, and Applications. *Chem. Rev.* **2015**, *115*, 11967–11998.

(64) May, F.; Marcon, V.; Hansen, M. R.; Grozema, F.; Andrienko, D. Relationship Between Supramolecular Assembly and Charge-Carrier Mobility in Perylenediimide Derivatives: The Impact of Side Chains. *J. Mater. Chem.* **2011**, *21*, 9538–9545.

(65) Ferlauto, L.; Liscio, F.; Orgiu, E.; Masciocchi, N.; Guagliardi, A.; Biscarini, F.; Samorì, P.; Milota, S. Enhancing the Charge Transport in Solution-Processed Perylene Di-imide Transistors via Thermal Annealing of Metastable Disordered Films. *Adv. Funct. Mater.* **2014**, *24*, 5503–5510.

(66) Resel, R.; Bainschab, M.; Pichler, A.; Dingemans, T.; Simbrunner, C.; Stangl, J.; Salzmänn, I. Multiple Scattering in Grazing-incidence X-Ray Diffraction: Impact on Lattice-Constant Determination in Thin Films. *J. Synchrotron Radiat.* **2016**, *23*, 729–734.

(67) Jones, B. A.; Ahrens, M. J.; Yoon, M.-H.; Facchetti, A.; Marks, T. J.; Wasielewski, M. R. High-Mobility Air-Stable n-Type Semiconductors with Processing Versatility: Dicyanoperylene-3,4,9,10-bis(dicarboximides). *Angew. Chem.* **2004**, *116*, 6523–6526.

(68) Musumeci, C.; Salzmänn, I.; Bonacchi, S.; Röthel, C.; Duhm, S.; Koch, N.; Samorì, P. The Relationship between Structural and Electrical Characteristics in Perylenecarboxydiimide-Based Nanoarchitectures. *Adv. Funct. Mater.* **2015**, *25*, 2501–2510.

(69) Björck, M.; Andersson, G. GenX: an Extensible X-ray Reflectivity Refinement Program Utilizing Differential Evolution. *J. Appl. Crystallogr.* **2007**, *40*, 1174–1178.

(70) Krauss, T. N.; Barrera, E.; de Oteyza, D. G.; Zhang, X. N.; Major, J.; Dehm, V.; Würthner, F.; Dosch, H. X-ray/Atomic Force Microscopy Study of the Temperature-Dependent Multilayer Structure of PTCDI-C₈ Films on SiO₂. *J. Phys. Chem. C* **2009**, *113*, 4502–4506.

(71) Heinemeyer, U.; Scholz, R.; Gisslén, L.; Alonso, M. I.; Ossó, J. O.; Garriga, M.; Hinderhofer, A.; Kytka, M.; Kowarik, S.; Gerlach, A.; et al. Exciton-Phonon Coupling in Diindenoperylene Thin Films. *Phys. Rev. B: Condens. Matter Mater. Phys.* **2008**, *78*, 085210.

(72) Hestand, N. J.; Yamagata, H.; Xu, B.; Sun, D.; Zhong, Y.; Harutyunyan, A. R.; Chen, G.; Dai, H.-L.; Rao, Y.; Spano, F. C. Polarized Absorption in Crystalline Pentacene: Theory vs Experiment. *J. Phys. Chem. C* **2015**, *119*, 22137–22147.

(73) Dieterle, J. The Influence of Dilution on Structural and Optical Properties of Organic Semiconductors. Ph.D. Thesis, University of Tübingen, Germany, 2016.

(74) Kasha, M.; Rawls, H. R.; Ashraf El-Bayoumi, M. The Exciton Model in Molecular Spectroscopy. *Pure Appl. Chem.* **1965**, *11*, 371–392.

(75) Austin, A.; Hestand, N. J.; McKendry, I. G.; Zhong, C.; Zhu, X.; Zdilla, M. J.; Spano, F. C.; Szarko, J. M. Enhanced Davydov Splitting in Crystals of a Perylene Diimide Derivative. *J. Phys. Chem. Lett.* **2017**, *8*, 1118–1123.

(76) Fulton, R. L.; Gouterman, M. Vibronic Coupling. I. Mathematical Treatment for Two Electronic States. *J. Chem. Phys.* **1961**, *35*, 1059–1071.

(77) Kelley, A. M. A Multimode Vibronic Treatment of Absorption, Resonance Raman, and Hyper-Rayleigh Scattering of Excitonically Coupled Molecular Dimers. *J. Chem. Phys.* **2003**, *119*, 3320–3331.

(78) Spano, F. C. The Spectral Signatures of Frenkel Polarons in H- and J-Aggregates. *Acc. Chem. Res.* **2010**, *43*, 429–439.

(79) Patterson, A. L. The Scherrer Formula for X-Ray Particle Size Determination. *Phys. Rev.* **1939**, *56*, 978–982.

(80) Broch, K.; Gerlach, A.; Lorch, C.; Dieterle, J.; Novák, J.; Hinderhofer, A.; Schreiber, F. Structure Formation in Perfluoropentacene:Diindenoperylene Blends and Its Impact on Transient Effects in the Optical Properties Studied in Real-Time During Growth. *J. Chem. Phys.* **2013**, *139*, 174709.

(81) Forker, R.; Fritz, T. Optical Differential Reflectance Spectroscopy of Ultrathin Epitaxial Organic Films. *Phys. Chem. Chem. Phys.* **2009**, *11*, 2142–2155.

(82) Heinemeyer, U.; Broch, K.; Hinderhofer, A.; Kytka, M.; Scholz, R.; Gerlach, A.; Schreiber, F. Real-Time Changes in the Optical Spectrum of Organic Semiconducting Films and Their Thickness Regimes during Growth. *Phys. Rev. Lett.* **2010**, *104*, 257401.

(83) Ghanbari, E.; Wagner, T.; Zeppenfeld, P. Layer-Resolved Evolution of Organic Thin Films Monitored by Photoelectron Emission Microscopy and Optical Reflectance Spectroscopy. *J. Phys. Chem. C* **2015**, *119*, 24174–24181.

(84) Gierschner, J.; Lüer, L.; Milián-Medina, B.; Oelkrug, D.; Egelhaaf, H.-J. Highly Emissive H-Aggregates or Aggregation-Induced Emission Quenching? The Photophysics of All-Trans para-Distyrylbenzene. *J. Phys. Chem. Lett.* **2013**, *4*, 2686–2697.

(85) Wykes, M.; Park, S. K.; Bhattacharyya, S.; Varghese, S.; Kwon, J. E.; Whang, D. R.; Cho, I.; Wannemacher, R.; Lüer, L.; Park, S. Y.; et al. Excited State Features and Dynamics in a Distyrylbenzene-Based Mixed Stack Donor–Acceptor Cocrystal with Luminescent Charge Transfer Characteristics. *J. Phys. Chem. Lett.* **2015**, *6*, 3682–3687.

(86) Muccini, M.; Murgia, M.; Biscarini, F.; Taliani, C. Morphology Controlled Energy Transfer in Conjugated Molecular Thin Films. *Adv. Mater.* **2001**, *13*, 355–358.

(87) Mei, P.; Murgia, M.; Taliani, C.; Lunedei, E.; Muccini, M. Luminescence Quantum Yield of Molecular Aggregates and Excitons in α -Sexithienyl Thin Films at Variable Temperature. *J. Appl. Phys.* **2000**, *88*, S158–S165.

- (88) Son, M.; Park, K. H.; Shao, C.; Würthner, F.; Kim, D. Spectroscopic Demonstration of Exciton Dynamics and Excimer Formation in a Sterically Controlled Perylene Bisimide Dimer Aggregate. *J. Phys. Chem. Lett.* **2014**, *5*, 3601–3607.
- (89) Schill, J.; Milroy, L.-G.; Lugger, J. A. M.; Schenning, A. P. H. J.; Brunsveld, L. Relationship between Side-Chain Polarity and the Self-Assembly Characteristics of Perylene Diimide Derivatives in Aqueous Solution. *ChemistryOpen* **2017**, *6*, 266–272.
- (90) Cook, R. E.; Phelan, B. T.; Kamire, R. J.; Majewski, M. B.; Young, R. M.; Wasielewski, M. R. Excimer Formation and Symmetry-Breaking Charge Transfer in Cofacial Perylene Dimers. *J. Phys. Chem. A* **2017**, *121*, 1607–1615.
- (91) Liu, H.; Shen, L.; Cao, Z.; Li, X. Covalently Linked Perylenetetracarboxylic Diimide Dimers and Trimers with Rigid “J-Type” Aggregation Structure. *Phys. Chem. Chem. Phys.* **2014**, *16*, 16399–16406.
- (92) Giaimo, J. M.; Lockard, J. V.; Sinks, L. E.; Scott, A. M.; Wilson, T. M.; Wasielewski, M. R. Excited Singlet States of Covalently Bound, Cofacial Dimers and Trimers of Perylene-3,4:9,10-bis(dicarboximide)s. *J. Phys. Chem. A* **2008**, *112*, 2322–2330.
- (93) Zykov, A.; Bommel, S.; Wolf, C.; Pithan, L.; Weber, C.; Beyer, P.; Santoro, G.; Rabe, J. P.; Kowarik, S. Diffusion and Nucleation in Multilayer Growth of PTCDI-C₈ Studied with *in situ* X-ray Growth Oscillations and Real-Time Small Angle X-ray Scattering. *J. Chem. Phys.* **2017**, *146*, 052803.
- (94) Lita, A. E.; Sanchez, J. E., Jr Effects of Grain Growth on Dynamic Surface Scaling During the Deposition of Al Polycrystalline Thin Films. *Phys. Rev. B* **2000**, *61*, 7692–7699.
- (95) Schwoebel, R. L.; Shipsey, E. J. Step Motion on Crystal Surfaces. *J. Appl. Phys.* **1966**, *37*, 3682–3686.
- (96) Ehrlich, G.; Hudda, F. G. Atomic View of Surface Self-Diffusion: Tungsten on Tungsten. *J. Chem. Phys.* **1966**, *44*, 1039–1049.
- (97) Desai, T. V.; Kish, E. R.; Woll, A. R.; Engstrom, J. R. Hyperthermal Growth of N,N'-Ditridecylperylene-3,4,9,10-tetracarboxylic Diimide on Self-Assembled Monolayers: Adsorption Dynamics and Sub- and Multilayer Thin Film Growth. *J. Phys. Chem. C* **2011**, *115*, 18221–18234.
- (98) Anger, F.; Glowatzki, H.; Franco-Cañellas, A.; Bürker, C.; Gerlach, A.; Scholz, R.; Sakamoto, Y.; Suzuki, T.; Koch, N.; Schreiber, F. Interface Dipole and Growth Mode of Partially and Fully Fluorinated Rubrene on Au(111) and Ag(111). *J. Phys. Chem. C* **2015**, *119*, 6769–6776.
- (99) Reisz, B.; Weimer, S.; Banerjee, R.; Zeiser, C.; Lorch, C.; Duva, G.; Dieterle, J.; Yonezawa, K.; Yang, J.-P.; Ueno, N.; et al. Structural, Optical, and Electronic Characterization of Perfluorinated Sexithiophene Films and Mixed Films with Sexithiophene. *J. Mater. Res.* **2017**, *32*, 1908–1920.
- (100) Savu, S.-A.; Abb, S.; Schundelmeier, S.; Saathoff, J. D.; Stevenson, J. M.; Tönshoff, C.; Bettinger, H. F.; Clancy, P.; Casu, M. B.; Chassé, T. Pentacene-Based Nanorods on Au(111) Single Crystals: Charge Transfer, Diffusion, and Step-Edge Barriers. *Nano Res.* **2013**, *6*, 449–459.
- (101) Rivnay, J.; Jimison, L. H.; Northrup, J. E.; Toney, M. F.; Noriega, R.; Lu, S.; Marks, T. J.; Facchetti, A.; Salleo, A. Large Modulation of Carrier Transport by Grain-Boundary Molecular Packing and Microstructure in Organic Thin Films. *Nat. Mater.* **2009**, *8*, 952–958.
- (102) Osuna, R. M.; Hernández, V.; Navarrete, J. T. L.; D'Oria, E.; Novoa, J. J. Theoretical Evaluation of the Nature and Strength of the F...F Intermolecular Interactions Present in Fluorinated Hydrocarbons. *Theor. Chem. Acc.* **2011**, *128*, 541–553.
- (103) Panini, P.; Chopra, D. Quantitative Insights into Energy Contributions of Intermolecular Interactions in Fluorine and Trifluoromethyl Substituted Isomeric N-phenylacetamides and N-methylbenzamides. *CrystEngComm* **2013**, *15*, 3711–3733.
- (104) Schuster, B.-E.; Basova, T. V.; Plyashkevich, V. A.; Peisert, H.; Chassé, T. Effects of Temperature on Structural and Morphological Features of CoPc and CoPcF₁₆ Thin Films. *Thin Solid Films* **2010**, *518*, 7161–7166.
- (105) Hird, M. Fluorinated Liquid Crystals – Properties and Applications. *Chem. Soc. Rev.* **2007**, *36*, 2070–2095.
- (106) Zugenmaier, P.; Duff, J.; Bluhm, T. L. Crystal and Molecular Structures of Six Differently with Halogen Substituted Bis(benzylimido) perylene. *Cryst. Res. Technol.* **2000**, *35*, 1095–1115.
- (107) Liscio, F.; Milita, S.; Albonetti, C.; D'Angelo, P.; Guagliardi, A.; Masciocchi, N.; Della Valle, R. G.; Venuti, E.; Brillante, A.; Biscarini, F. Structure and Morphology of PDI8-CN₂ for n-Type Thin-Film Transistors. *Adv. Funct. Mater.* **2012**, *22*, 943–953.
- (108) Spano, F. Analysis of the UV/Vis and CD Spectral Line Shapes of Carotenoid Assemblies: Spectral Signatures of Chiral H-Aggregates. *J. Am. Chem. Soc.* **2009**, *131*, 4267–4278.
- (109) Gisslén, L.; Scholz, R. Crystallography of Perylene Pigments: Influence of an Enlarged Polyaromatic Core Region. *Phys. Rev. B: Condens. Matter Mater. Phys.* **2011**, *83*, 155311.
- (110) Oettel, M.; Klopotek, M.; Dixit, M.; Empting, E.; Schilling, T.; Hansen-Goos, H. Monolayers of hard rods on planar substrates. I. Equilibrium. *J. Chem. Phys.* **2016**, *145*, 074902.